HAL
open science

Manifold Topology Divergence: a Framework for Comparing Data Manifolds

Serguei Barannikov, Ilya Trofimov, Grigorii Sotnikov, Ekaterina Trimbach, Alexander Korotin, Alexander Filippov, Evgeny Burnaev

To cite this version:

Serguei Barannikov, Ilya Trofimov, Grigorii Sotnikov, Ekaterina Trimbach, Alexander Korotin, et al.. Manifold Topology Divergence: a Framework for Comparing Data Manifolds. Advances in Neural Information Processing Systems, 2021, 10.48550/arXiv.2106.04024 . hal-03418125

HAL Id: hal-03418125

https://hal.science/hal-03418125v1

Submitted on 6 Nov 2021

HAL is a multi-disciplinary open access archive for the deposit and dissemination of scientific research documents, whether they are published or not. The documents may come from teaching and research institutions in France or abroad, or from public or private research centers.

L'archive ouverte pluridisciplinaire **HAL**, est destinée au dépôt et à la diffusion de documents scientifiques de niveau recherche, publiés ou non, émanant des établissements d'enseignement et de recherche français ou étrangers, des laboratoires publics ou privés.

Manifold Topology Divergence: a Framework for Comparing Data Manifolds

Serguei Barannikov
Skolkovo Institute of Science and Technology
Moscow, Russia
CNRS, IMJ, Paris University, France

Ilya Trofimov
Skolkovo Institute of Science and Technology
Moscow, Russia

Grigorii Sotnikov
Skolkovo Institute of Science and Technology
Moscow, Russia

Ekaterina Trimbach
Moscow Institute of Physics and Technology
Moscow, Russia

Alexander Korotin
Skolkovo Institute of Science and Technology
Moscow, Russia

Alexander Filippov
Huawei Noah's Ark Lab

Evgeny Burnaev
Skolkovo Institute of Science and Technology,
Artificial Intelligence Research Institute (AIRI),
Moscow, Russia

Abstract

We develop a framework for comparing data manifolds, aimed, in particular, towards the evaluation of deep generative models. We describe a novel tool, Cross-Barcode(P,Q), that, given a pair of distributions in a high-dimensional space, tracks multiscale topology spacial discrepancies between manifolds on which the distributions are concentrated. Based on the Cross-Barcode, we introduce the Manifold Topology Divergence score (MTop-Divergence) and apply it to assess the performance of deep generative models in various domains: images, 3D-shapes, time-series, and on different datasets: MNIST, Fashion MNIST, SVHN, CIFAR10, FFHQ, chest X-ray images, market stock data, ShapeNet. We demonstrate that the MTop-Divergence accurately detects various degrees of mode-dropping, intra-mode collapse, mode invention, and image disturbance. Our algorithm scales well (essentially linearly) with the increase of the dimension of the ambient high-dimensional space. It is one of the first TDA-based practical methodologies that can be applied universally to datasets of different sizes and dimensions, including the ones on which the most recent GANs in the visual domain are trained. The proposed method is domain agnostic and does not rely on pre-trained networks.

1 Introduction

Geometric perspective in working with data distributions has been pervasive in machine learning [5, 8, 12, 10, 23, 20]. Reconstruction of the data from observing only a subset of its points has made a significant step forward since the invention of Generative Adversarial Networks (GANs) [13]. Despite the exceptional success that deep generative models achieved, there still exists a longstanding challenge of good assessment of the generated samples quality and diversity [7].

35th Conference on Neural Information Processing Systems (NeurIPS 2021).

For images, the Fréchet Inception Distance (FID) [16] is the most popular GAN evaluation measure. However, FID is limited only to 2D images since it relies on pre-trained on ImageNet "Inception" network. FID unrealistically approximates point clouds by Gaussians in embedding space; also, FID is biased [6]. Surprisingly, FID can't be applied to compare adversarial and non-adversarial generative models since it is overly pessimistic to the latter ones [28].

The evaluation of generative models is about comparing two *point clouds*: the true data cloud P_{data} and the model (generated) cloud Q_{model}. In view of the commonly assumed Manifold Hypothesis [5, 12], we develop a topology-based measure for comparing two manifolds: the true data manifold M_{data} and the model manifold M_{model}, by analysing samples $P_{\text{data}} \subset M_{\text{data}}$ and $Q_{\text{model}} \subset M_{\text{model}}$.

Contribution. In this work, we make the following contributions:

1. We introduce a new tool: Cross-Barcode(P, Q). For a pair of point clouds P and Q, the Cross-Barcode(P, Q) records the differences in multiscale topology between two manifolds approximated by the point clouds;
2. We propose a new measure for comparing two data manifolds approximated by point clouds: Manifold Topology Divergence (MTop-Div);
3. We apply the MTop-Div to evaluate performance of GANs in various domains: 2D images, 3D shapes, time-series. We show that the MTop-Div correlates well with domain-specific measures and can be used for model selection. Also it provides insights about evolution of generated data manifold during training;
4. We have compared the MTop-Div against 7 established evaluation methods: FID, discriminative score, MMD, JSD, 1-coverage, IMD and Geometry score and found that MTop-Div is able to capture subtle differences in data geometry;
5. We have essentially overcame the known TDA scalability issues and in particular have carried out the MTop-Div calculations on most recent datasets such as FFHQ, with dimensions D up to 10^7.

The source code is available at `https://github.com/IlyaTrofimov/MTopDiv`.

Related work. GANs try to recover the true data distribution via a min-max game where two players, typically represented by deep neural networks, called Discriminator and Generator, compete by optimizing the common objective. Training curves are not informative since generator and discriminator counter each other, thus, the loss values are often meaningless. Several other measures were introduced to estimate the quality of GANs. However, there is no consensus which of them best captures strengths and limitations of the models and can be used for the fair model selection. The likelihood in Parzen window works poorly in high-dimensional spaces and does not correlate with the visual quality of generated samples [30]. The Inception Score (IS) [29] measures both the discriminability and diversity of generated samples. It relies on the pre-trained Inception network and is limited to 2D images domain. While IS correlates with visual image quality, it ignores the true data distribution, doesn't detect mode dropping and is sensitive to image resolution. The Fréchet Inception Distance (FID) [16] is a distance between two multivariate Gaussians. These Gaussians approximate the features of generated and true data extracted from the last hidden layer of the pretrained Inception network. Similar variant is KID [6] which computes MMD distance between two distributions of features. The work [14] proposed to use the Duality Gap, a notion from the game theory, as a domain agnostic measure for GAN evaluation. Another variant of a measure inspired by game theory was proposed in [27]. Conventional precision and recall measures can be also used [22, 21]. Accurate calculation of precision and recall is limited to simple datasets from low-dimensional manifolds. The *Geometry Score* (GScore) [19] is the L2-distance between mean Relative Living Times (RLT) of topological features calculated for the model distribution and the true data distribution. The GScore is domain agnostic, does not involve auxiliary pretrained networks and is not limited to 2D images. However, GScore is not sensitive even to some simple transformations - like constant shift, dilation, or reflection (see our Fig. 2, 4). The barcodes in GScore are calculated approximately, based only on the approximate witness complexes on 64 landmark points sampled from each distribution. That's why the procedure is stochastic and should be repeated several thousand times for averaging. Thus, the calculation of GScore can be prohibitively long for large datasets. We also refer reader to the comprehensive survey [7].

2 Cross-Barcode and Manifold Topology Divergence

2.1 Multiscale simplicial approximation of manifolds

According to the well-known Manifold Hypothesis [12] the support of the data distribution $\mathcal{P}_{\text{data}}$ is often concentrated on a low-dimensional manifold M_{data}. We construct a framework for comparing numerically such distribution $\mathcal{P}_{\text{data}}$ with a similar distribution $\mathcal{Q}_{\text{model}}$ concentrated on a manifold M_{model}. Such distribution $\mathcal{Q}_{\text{model}}$ is produced, for example, by a generative deep neural network in one of applications' scenarios. The immediate difficulty here is that the manifold M_{data} is unknown and is described only through discrete sets of samples from the distribution $\mathcal{P}_{\text{data}}$. One standard approach to resolve this difficulty is to approximate the manifold M_{data} by simplices with vertices given by the sampled points. The simplices approximating the manifold are picked based on proximity information given by the pairwise distances between sampled points [5, 25]. The standard approach is to fix a threshold $r > 0$ and to take the simplices whose edges do not exceed the threshold r. The choice of threshold is essential here since if it is too small, then only the initial points, i.e., separated from each other 0-dimensional simplices, are allowed. And if the threshold is too large, then all possible simplices with sampled points as vertices are included and their union is simply the big blob representing the convex hull of the sampled points. Instead of trying to guess the right value of the threshold, the standard recent approach is to study all thresholds at once. This can be achieved thanks to the mathematical tool, called barcode [2, 10], that quantifies the evolution of topological features over multiple scales. For each value of r the barcode describes the topology, namely the numbers of holes or voids of different dimensions, of the union of all simplices included up to the threshold r.

2.2 Measuring the differences in simplicial approximation of two manifolds

However, to estimate numerically the degree of similarity between the manifolds $M_{\text{model}}, M_{\text{data}} \subset \mathbb{R}^D$, it is important not just to know the numbers of topological features across different scales for simplicial complexes approximating $M_{\text{model}}, M_{\text{data}}$, but to be able to verify that the similar topological features are located at similar places and appear at similar scales.

Our method measures the differences in the simplicial approximation of the two manifolds, represented by samples P and Q, by constructing sets of simplices, describing discrepancies between the two manifolds. To construct these sets of simplices we take the edges connecting $P-$points with $Q-$points, and also $P-$points between them, ordered by their length, and start adding these edges one by one, beginning from the smallest edge and gradually increasing the threshold, see Figure 1. We add also the triangles and $k-$simplices at the threshold when all their edges have been added. It is assumed that all edges between $Q-$points were already in the initial set. We track in this process the births and the deaths of topological features, where the topological features are allowed here to have boundaries on any simplices formed by $Q-$points. The longer the lifespan of the topological feature across the change of threshold the bigger the described by this feature discrepancy between the two manifolds.

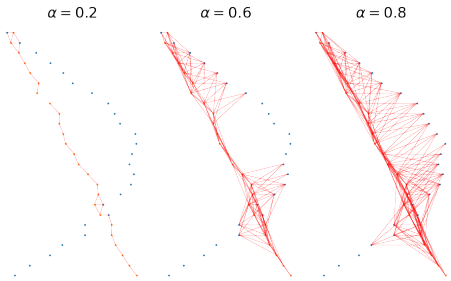

Figure 1: Edges(red) connecting $P-$points(red) with $Q-$points(blue), and also $P-$points between them, are added for three thresholds: $\alpha = 0.2, 0.4, 0.6$

Homology is a tool that permits to single out topological features that are similar, and to decompose any topological feature into a sum of basic topological features. More specifically, in our case, a $k-$cycle is a collection of $k-$simplices formed by $P-$ and $Q-$ points, such that their boundaries cancel each other, perhaps except for the boundary simplices formed only by $Q-$points. For example, a cycle of dimension $k = 1$ corresponds to a path connecting a pair of $Q-$points and consisting of edges passing through a set of $P-$points. A cycle which is a boundary of a set of $(k+1)-$simplices is considered trivial. Two cycles are topologically equivalent if they differ by a boundary, and by collection of simplices formed only by $Q-$points. A union of cycles is again a cycle. Each cycle can be represented by a vector in the vector space where each simplex corresponds to a generator. In practice, the vector space over $\{0, 1\}$ is used most often. The union of cycles corresponds to the sum of vectors. The homology vector space H_k is defined as the factor of the vector space of all $k-$cycles

modulo the vector space of boundaries and cycles consisting of simplices formed only by $Q-$points. A set of vectors forming a basis in this factor-space corresponds to a set of basic topological features, so that any other topological feature is equivalent to a sum of some basic features.

The homology are also defined for manifolds and for arbitrary topological spaces. This definition is technical and we have to omit it due to limited space, and to refer to e.g. [15, 24] for details. The relevant properties for us are the following. For each topological space X the vector spaces $H_k(X)$, $k = 0, 1 \ldots$, are defined. The dimension of the vector space H_k equals to the number of independent $k-$dimensional topological features (holes,voids etc). An inclusion $Y \subset X$ induces a natural map $H_k(Y) \to H_k(X)$

In terms of homology, we would like to verify that not just the dimensions of homology groups $H_*(M_{\text{model}})$ and $H_*(M_{\text{data}})$ are the same but that more importantly the natural maps:

$$\varphi_r : H_*(M_{\text{model}} \cap M_{\text{data}}) \to H_*(M_{\text{model}}) \tag{1}$$

$$\varphi_p : H_*(M_{\text{model}} \cap M_{\text{data}}) \to H_*(M_{\text{data}}) \tag{2}$$

induced by the embeddings are as close as possible to isomorphisms. The homology of a pair is the tool that measures how far such maps are from isomorphisms. Given a pair of topological spaces $Y \subset X$, the homology of a pair $H_*(X, Y)$ counts the number of independent topological features in X that cannot be deformed to a topological feauture in Y plus independent topological features in Y that, after the embedding to X, become deformable to a point. An equivalent description, the homology of a pair $H_*(X, Y)$ counts the number of independent topological features in the factor-space X/Y, where all points of Y are contracted to a single point. The important fact for us is that the map, induced by the embedding, $H_*(Y) \to H_*(X)$ is an isomorphism if and only if the homology of the pair $H_*(X, Y)$ are trivial. Moreover the embedding of simple simplicial complexes $Y \subset X$ is an equivalence in homotopy category, if and only if the homology of the pair $H_*(X, Y)$ are trivial [33].

To define the counterpart of this construction for manifolds represented by point clouds, we employ the following strategy. Firstly, we replace the pair $(M_{\text{model}} \cap M_{\text{data}}) \subset M_{\text{model}}$ by the equivalent pair $M_{\text{model}} \subset (M_{\text{data}} \cup M_{\text{model}})$ with the same factor-space. Then, we represent $(M_{\text{data}} \cup M_{\text{model}})$ by the union of point clouds $P \cup Q$, where the point clouds P, Q are sampled from the distributions $\mathcal{P}_{\text{data}}$, $\mathcal{Q}_{\text{model}}$. Our principal claim here is that taking topologically the quotient of $(M_{\text{data}} \cup M_{\text{model}})$ by M_{model} is equivalent in the framework of multiscale analysis of topological features to the following operation on the matrix $m_{P \cup Q}$ of pairwise distances of the cloud $P \cup Q$: **we set to zero all pairwise distances within the subcloud Q** $\subset (P \cup Q)$.

2.3 Cross-Barcode (P,Q)

Let $P = \{p_i\}$, $Q = \{q_j\}$, $p_i, q_j \in \mathbb{R}^D$ are two point clouds sampled from two distributions $\mathcal{P}$, $\mathcal{Q}$. To define Cross-Barcode(P, Q) we construct first the following filtered simplicial complex. Let $(\Gamma_{P \cup Q}, m_{(P \cup Q)/Q})$ be the weighted graph with the distance-like weights on edges defined as the complete graph on the union of point clouds $P \cup Q$ with the distance matrix given by the pairwise distance in $\mathbb{R}^D$ for the pairs of points (p_i, p_j) or (p_i, q_j) and with all pairwise distances within the cloud Q that we set to zero. Our filtered simplicial complex is the Vietoris-Rips complex of $(\Gamma_{P \cup Q}, m_{(P \cup Q)/Q})$.

Recall that given such a graph Γ with matrix m of pairwise distances between vertices and a parameter $\alpha > 0$, the Vietoris-Rips complex $R_\alpha(\Gamma, m)$ is the abstract simplicial complex with simplices that correspond to the non-empty subsets of vertices of Γ whose pairwise distances are less than α as measured by m. Increasing parameter α adds more simplices and this gives a nested family of collections of simplices know as filtered simplicial complex. Recall that a **simplicial complex** is described by a set of vertices $V = \{v_1, \ldots, v_N\}$, and a collection of $k-$simplices S, i.e. $(k+1)-$elements subsets of the set of vertices V, $k \geq 0$. The set of simplices S should satisfy the condition that for each simplex $s \in S$ all the $(k-1)$-simplices obtained by the deletion of a vertex from the subset of vertices of s belong also to S. The **filtered simplicial complexes** is the family of simplicial complexes S_α with nested collections of simplices: for $\alpha_1 < \alpha_2$ all simplices of S_{α_1} are also in S_{α_2}.

At the initial moment, $\alpha = 0$, the simplicial complex $R_\alpha(\Gamma_{P \cup Q}, m_{(P \cup Q)/Q})$ has trivial homology H_k for all $k > 0$ since it contains all simplices formed by $Q-$points. The dimension of the $0-$th

homology equals at $\alpha = 0$ to the number of $P-$points, since no edge between them or between a $P-$point and a $Q-$point is added at the beginning. As we increase α, some cycles, holes or voids appear in our complex R_α. Then, some combinations of these cycles disappear. The **persistent homology** principal theorem [2, 37] implies that it is possible to choose the set of generators in the homology of filtered complexes $H_k(R_\alpha)$ across all the scales α such that each generator appears at its specific "birth" time and disappears at its specific "death" time. These sets of "birth" and "deaths" of topological features in R_α are registered in **Barcode** of the filtered complex.

Definition. The Cross-Barcode$_i(P,Q)$ is the set of intervals recording the "births" and "deaths" times of $i-$dimensional topological features in the filtered simplicial complex $R_\alpha(\Gamma_{P\cup Q}, m_{(P\cup Q)/Q})$.

Examples of Cross-Barcode$_i(P,Q)$ are shown on Fig. 2, 11, 14, 17, 18. Topological features with longer "lifespan" are considered essential. The topological features with "birth"="death" are trivial by definition and do not appear in Cross-Barcode$_*(P,Q)$.

2.4 Basic properties of Cross-Barcode$_*$(P,Q)

Proposition 1. Here is a list of basic properties of Cross-Barcode$_*(P,Q)$:

- if the two clouds coincide then Cross-Barcode$_*(P,P) = \varnothing$;
- for $Q = \varnothing$, Cross-Barcode$_*(P,\varnothing) =$ Barcode$_*(P)$, the barcode of the single point cloud P itself;
- the norm of Cross-Barcode$_i(P,Q)$, $i \geq 0$, is bounded from above by the Hausdorff distance

$$\|\text{Cross-Barcode}_i\,(P,Q)\|_B \leq d_H(P,Q). \tag{3}$$

The proof is given in appendix.

2.5 The Manifold Topology Divergence (MTop-Div)

The bound from eq.(3) and the equality Cross-Barcode$_*(P,P) = \varnothing$ imply that the closeness of Cross-Barcode$_*(P,Q)$ to the empty set is a natural measure of discrepancy between $\mathcal{P}$ and $\mathcal{Q}$. Each Cross-Barcode$_i(P,Q)$ is a list of intervals describing the persistent homology H_i. To measure the closeness to the empty set, one can use segments' statistics: sum of lengths, sum of squared lengths, number of segments, the maximal length (H$_i$ max) or specific quantile. We assume that various characteristics of different H_i could be useful in various cases, but the cross-barcodes for H_0 and H_1 can be calculated relatively fast.

Our **MTop-Divergence**($\mathcal{P}$, $\mathcal{Q}$) is based on the sum of lengths of segments in Cross-Barcode$_1(P,Q)$, see section 2.6 for details. The sum of lengths of segments in Cross-Barcode$_1(P,Q)$ has an interesting interpretation via the Earth Mover's Distance. Namely, it is easy to prove (see Appendix B.2) that EM-Distance between the Relative Living Time histogram for Cross-Barcode$_1(P,Q)$ and the histogram of the empty barcode, multiplied by the parameter α_{max} from the definition of RLT, see e.g. [19], coincides with the sum of lengths of segments in H_1. This ensures the standard good stability properties of this quantity.

Our metrics can be applied in two settings: to a pair of distributions $\mathcal{P}_{\text{data}}$, $\mathcal{Q}_{\text{model}}$, in which case we denote our score MTop-Div(D,M), and to a pair of distributions $\mathcal{Q}_{\text{model}}$, $\mathcal{P}_{\text{data}}$, in which case our score is denoted MTop-Div(M,D). These two variants of the Cross-Barcode, and of the MTop-Divergence are related to the concepts of precision and recall. These two variants can be analyzed separately or combined together, e.g. averaged.

2.6 Algorithm

To calculate the score that evaluates the similitude between two distributions, we employ the following algorithm. First, we compute Cross-Barcode$_1(P,Q)$ on point clouds P, Q of sizes b_P, b_Q sampled from the two distributions $\mathcal{P}$, $\mathcal{Q}$. For this we calculate the matrices m_P, $m_{P,Q}$ of pairwise distances within the cloud P and between clouds P and Q. Then the algorithm constructs the Vietoris-Rips filtered simplicial complex from the matrix $m_{(P\cup Q)/Q}$ which is the matrix of pairwise distances in $P \cup Q$ with the pairs of points from cloud Q block replaced by zeroes and with other blocks given by m_P, $m_{P,Q}$. Next step is to calculate the barcode of the constructed filtered simplicial complex. This step and the previous step constructing the filtered complex from the matrix $m_{(P\cup Q)/Q}$ can

Algorithm 1 Cross-Barcode$_i(P, Q)$

Input: $m[P, P]$, $m[P, Q]$: matrices of pairwise distances within point cloud P, and between point clouds P and Q
Require: VR(M): function computing filtered complex from pairwise distances matrix M
Require: B(C, i): function computing persistence intervals of filtered complex C in dimension i
$b_Q \leftarrow$ number of columns in matrix $m[P, Q]$
$m[Q, Q] \leftarrow$ zeroes(b_Q, b_Q)
$M \leftarrow \begin{pmatrix} m[P,P] & m[P,Q] \\ m[P,Q] & m[Q,Q] \end{pmatrix}$
Cross-Barcode$_i \leftarrow$ B(VR$(M), i)$
Return: list of intervals **Cross-Barcode**$_i(P, Q)$ representing "births" and "deaths" of topological discrepancies

Algorithm 2 MTop-Divergence($\mathcal{P}$, $\mathcal{Q}$), see section 2.6 for details, default suggested values: $b_\mathcal{P} = 1000$, $b_\mathcal{Q} = 10000$, $n = 100$

Input: $X_\mathcal{P}$, $X_\mathcal{Q}$: $N_\mathcal{P} \times D$, $N_\mathcal{Q} \times D$ arrays representing datasets
for $j = 1$ **to** n **do**
$P_j \leftarrow$ random choice($X_\mathcal{P}$,$b_\mathcal{P}$)
$Q_j \leftarrow$ random choice($X_\mathcal{Q}$,$b_\mathcal{Q}$)
$\mathcal{B}_j \leftarrow$ list of intervals Cross-Barcode$_1(P_j, Q_j)$ calculated by Algorithm1
$mtd_j \leftarrow$ sum of lengths of all intervals in $\mathcal{B}_j$
end for
MTop-Divergence($\mathcal{P}$, $\mathcal{Q}$) $\leftarrow$ mean(mtd)
Return: number **MTop-Divergence**($\mathcal{P}$, $\mathcal{Q}$) representing discrepancy between the distributions $\mathcal{P}$, $\mathcal{Q}$

be done using one of the fast scripts[1], some of them are optimized for GPU acceleration, see e.g. [35, 4]. The calculation of barcode from the filtered complex is based on the persistence algorithm bringing the filtered complex to its "canonical form" ([2]). Next, sum of lengths or one of other numerical characteristcs of Cross-Barcode$_1(P, Q)$ is computed. Then this computation is run a sufficient number of times to obtain the mean value of the picked characteristic. In our experiments we have found that for common datasets the number of times from 10 to 100 is generally sufficient. Our method is summarized in the Algorithms 1 and 2.

Complexity. The Algorithm 1 requires computation of the two matrices of pairwise distances $m[P, P]$, $m[P, Q]$ for a pair of samples $P \in \mathbb{R}^{b_\mathcal{P} \times D}$, $Q \in \mathbb{R}^{b_\mathcal{Q} \times D}$ involving $O(b_\mathcal{P}^2 D)$ and $O(b_\mathcal{P} b_\mathcal{Q} D)$ operations. After that, the complexity of the computation of barcode does not depend on the dimension D of the data. Generally the persistence algorithm is at worst cubic in the number of simplices involved. In practice, the boundary matrix is sparse in our case and thanks also to the GPU optimization, the computation of cross-barcode takes similar time as in the previous step on datasets of big dimensionality. Since only the discrepancies in manifold topology are calculated, the results are quite robust and a relatively low number of iterations is needed to obtain accurate results. Since the algorithm scales linearly with D it can be applied to the most recent datasets with D up to 10^7. For example, for $D = 3.15 \times 10^6$, and batch sizes $b_\mathcal{P} = 10^3, b_\mathcal{Q} = 10^4$, on NVIDIA TITAN RTX the time for GPU accelerated calculation of pairwise distances was 15 seconds, and GPU-accelerated calculation of Cross-Barcode$_1(P, Q)$ took 30 seconds.

3 Experiments

We examine the ability of MTop-Div to measure quality of generative models trained on various datasets. Firstly, we illustrate the behaviour of MTop-Div on simple synthetic datasets (rings (Fig.2), disks (Fig. 13)). Secondly, we show that MTop-Div is superior to the GScore, another topology-based GAN quality measure. We carry out experiments with a mixture of Gaussians, MNIST, CIFAR10, X-ray images, FFHQ. The performance of MTop-Div is on par with FID. For images, MTop-Div is always calculated in pixel space without utilizing pre-trained networks. Thirdly, we apply MTop-Div to GANs from non-image domains: 3D shapes and time-series, where FID is not applicable. We show that MTop-Div agrees with domain-specific measures, such as JSD, MMD, Coverage, discriminative score, but MTop-Div better captures evolution of generated data manifold during training [2].

3.1 Simple synthetic datasets in 2D

As illustrated on Fig. 2 the GScore does not respond to shifts of the distributions' relative position.

[1] Persistent Homology Computation (wiki)
[2] we additionally calculated IMD [31] for the pairs of point clouds from our experiments, see Appendix E.

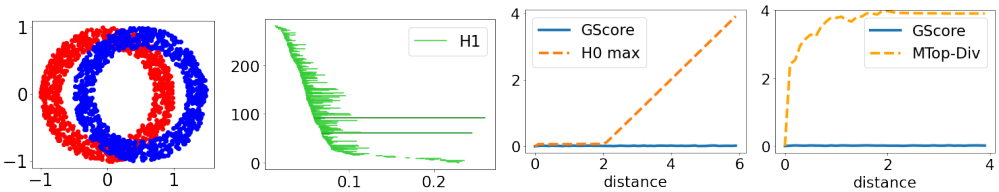

Figure 2: MTop-Div and H0 max compared with GScore, for two ring clouds of 1000 points, as function of d =distance between ring centers, the Cross-Barcode$_1(P, Q)$ is shown at $d = 0.5$

3.2 Mode-Droping on Gaussians

One of common tasks to assess GAN's performance is measuring it's ability to uncover the variety of modes in the data distribution. A common benchmark for this problem is a mixture of Gaussians, see Fig. 3. We trained two generators with very different performance: original GAN, which managed to capture all 5 modes of the distribution and WGAN-GP, which have only covered poorly two. However, the Geometry score is not sensitive to such a difference since two point clouds have the same RLT histogram. While the MTop-Div is sensitive to such a difference.

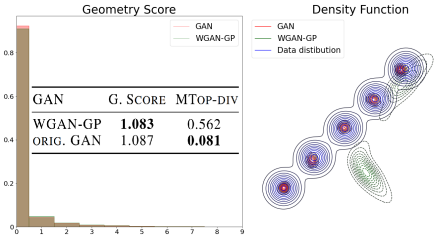

GAN	G. Score	MTop-Div
WGAN-GP	**1.083**	0.562
Orig. GAN	1.087	**0.081**

Figure 3: Difficulty of the Geometry Score to detect the mode dropping.

3.3 Digit flipping on MNIST

Figure 4 shows an experiment with MNIST dataset. We compare two point clouds: "5"s vs. vertically flipped "5"s (resembling rather "2"s). These two clouds are indistinguishable for Geometry Score, while the MTop-Div is sensitive to such flip since it depends on the relative position of the two clouds.

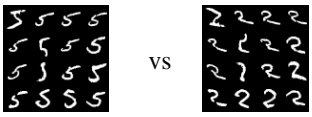

Geometry Score = 0.0
MTop-Div = 6154.0

Figure 4: Two point clouds:"5"s from MNIST vs. vertically flipped "5"s from MNIST (resembling rather "2"s). The two clouds are indistinguishable for Geometry Score, while the MTop-Div is sensitive to such flip as it depends on the positions of clouds with respect to each other.

3.4 Synthetic modifications of CIFAR10

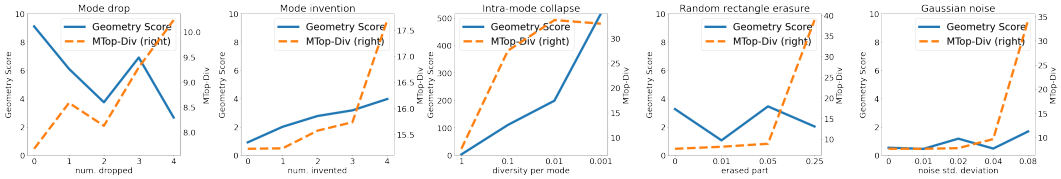

Figure 5: Experiment with modifications of CIFAR10. The disturbance level rises from zero to a maximum. Ideally, the quality score should monotonically increase with the disturbance level.

We evaluate the proposed MTop-Div(D,M) using a benchmark with the controllable disturbance level. We take CIFAR10 and apply the following modifications. Firstly, we emulate common issues in GAN: mode drop, mode invention and mode collapse by doing class drop, class addition and intra-class collapse (removal of objects within a class). Secondly, we apply two disturbance types: erasure of a random rectangle and a Gaussian noise. As 'real' images we use the test set from CIFAR10, as 'generated' images - a subsample of the train set with applied modifications. The size of the later always equals the test set size. Figure 5 shows the results. Ideally, the quality measure should monotonically increase with the disturbance level. We conclude that Geometry Score is monotone only for 'mode invention' and 'intra-mode collapse' while MTop-Div(D,M) is almost monotone for all the cases. The average Kendall-tau rank correlation between MTop-Div(D,M) and disturbance level is 0.89, while for Geometry Score the rank correlation is only 0.36. FID performs well on this

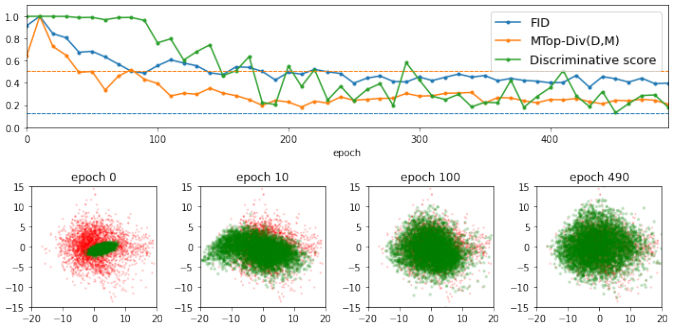

Figure 6: Training process of GAN applied to chest X-ray data. **Top**: normalized quality measures FID, MTop-Div, Disc. score vs. epoch. Each measure is divided by it's maximum value: max. FID = 304, max MTop-Div = 21, max. Disc.score = 0.5. Lower is better. Dashed horizontal lines depict comparison of real COVID-positive and COVID-neg. chest X-rays. **Bottom**: PCA projections of real objects (red) and generated objects (green).

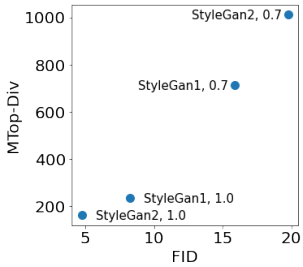

Figure 7: Comparison of the quality measures, FID vs MTop-Div, on StyleGAN, StyleGAN2 trained on FFHQ with different truncation levels. MTop-Div(M,D) is monotonically increasing in good correlation with FID.

benchmark, not shown on Figure 5 for ease of perception. Additionally, we calculated MTop-Div for higher order Cross-Barcodes, see Appendix D.

3.5 GAN model selection

We trained WGAN and WGAN-GP on various datasets: CIFAR10, SVHN, MNIST, Fashion-MNIST and evaluated their quality, see Table 1. Experimental data show that the ranking between WGAN and WGAN-GP is consistent for FID and MTop-Div.

Table 1: MTop-Div is consistent with FID for model selection of GAN's trained on various datasets.

Dataset	FID		MTop-Div(D,M)	
	WGAN	WGAN-GP	WGAN	WGAN-GP
CIFAR10	**154.6**	399.2	**353.1**	1637.4
SVHN	**101.6**	154.7	**332.0**	963.2
MNIST	31.8	**22.0**	2042.8	**1526.1**
FashionMNIST	52.9	**35.1**	919.6	**660.4**

3.6 Experiments with StyleGAN

We evaluated the performance of StyleGAN [17] and StyleGAN2 [18] generators trained on the FFHQ dataset[3]. We generated 20×10^3 samples with two truncation levels: $\psi = 0.7, 1.0$ and compared them with 20×10^3 samples from FFHQ. The truncation trick is known to improve average image quality but decrease image variance. Figure 7 show the results (see also Table 2 in Appendix for more data). Thus, the ranking via MTop-Div(M, D) is consistent with FID. We also tried to calculate Geometry Score but found that it takes a prohibitively long time.

3.7 Chest X-rays generation for COVID-19 detection

Waheen et al. [32] described how to apply GANs to improve COVID-19 detection from chest X-ray images. Following [32], we trained an ACGAN [26] on a dataset consisting of chest X-rays of COVID-19 positive and healthy patients [4]. Next, we studied the training process of ACGAN. Every 10'th epoch we evaluated the performance of ACGAN by comparing real and generated COVID-19 positive chest X-ray images. That is, we calculated FID, MTop-Div(D,M) and a baseline measure -

[3] `https://github.com/NVlabs/ffhq-dataset` (CC-BY 2.0 License)

[4] We used the ACGAN implementation `https://github.com/clvrai/ACGAN-PyTorch`, (MIT License) and chest X-ray data was from `https://www.kaggle.com/tawsifurrahman/covid19-radiography-database` (Kaggle Data License)

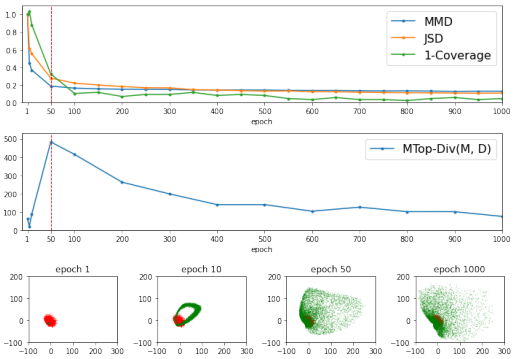

Figure 8: Training process of GAN applied to 3D shapes. **Top, middle**: quality measures MMD, JSD, 1-Coverage, MTop-Div vs. epoch. Each quality measure is normalized, that is, divided by its value at the first epoch. Lower is better. **Bottom**: PCA projection of real objects (red) and generated objects (green). **Vertical red line** (epoch 50) depicts the moment, when the manifold of generated objects "explodes" and becomes much more diverse.

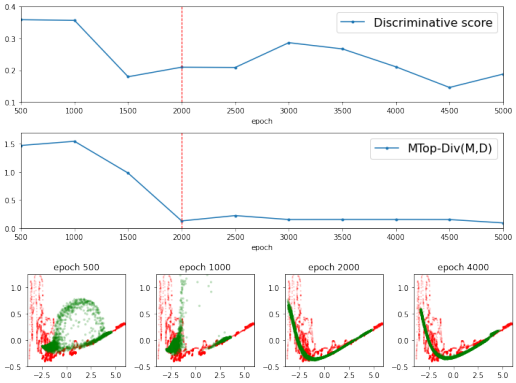

Figure 9: Training dynamics of TimeGAN applied to market stock data. **Top**: discriminative score vs. epoch, MTop-Div vs. epoch. Lower is better. **Bottom**: PCA projection of real time-series (red) and generated time-series (green). **Vertical red line** (epoch 2000) depicts the moment when manifolds of real and generated objects become close.

discriminative score [5] of a CNN trained to distinguish real vs. generated data. The MTop-Div agrees with FID and the discriminative score. PCA projections show that generated data approximates real data well. Figure 20 in Appendix presents real and generated images.

Additionally, we compared real COVID-positive and COVID-negative chest X-ray images, see horizontal dashed lines at Fig. 6. Counterintuitively, for FID real COVID-positive images are closer to real COVID-negative ones than to generated COVID-positive images; probably because FID is overly sensitive to textures. At the same time, evaluation by MTop-Div is consistent.

3.8 3D shapes generation

We use the proposed MTop-Div score to analyze the training process of the GAN applied to 3D shapes, represented by 3D point clouds [1]. For training, we used 6778 objects of the "chair" class from ShapeNet [9]. We trained GAN for 1000 epochs and tracked the following standard quality measures: Minimum Matching Distance (MMD), Coverage, and Jensen-Shannon Divergence (JSD) between marginal distributions. To understand the training process in more details, we computed PCA decomposition of real and generated objects (Fig. 8, bottom). For computing PCA, each object (3D point cloud) was represented by a vector of point frequencies attached to the 3-dimensional 28^3 grid. Figure 8, top, shows that conventional metrics (MMD, JSD, Coverage) doesn't represent the training process adequately. While these measures steadily improve, the set of generated objects dramatically changes. At epoch 50, the set of generated objects (green) "explodes" and becomes much more diverse, covering a much larger space than real objects (red). Conventional quality measures (MMD, JSD, Coverage) ignore this shift while MTop-Div has a peak at this point. Next, we evaluated the final quality of GAN by training a classifier to distinguish real and generated object. A simple MLP with 3 hidden layers showed accuracy 98%, indicating that the GAN poorly approximates the manifold of real objects. This result is consistent with MTop-Div: at epoch 1000 it is even larger than at epoch 1.

3.9 Time series generation

Next, we analyze training dynamics of TimeGAN [34] tailored to multivariate time-series generation. We followed the experimental protocol from [34] and used the daily historical market stocks data

[5] Discriminative score equals accuracy minus 0.5. MTop-Div better correlates with the discriminative score than FID: 0.75 vs. 0.66.

from 2004 to 2019, including as features the volume, high, low, opening, closing, and adjusted closing prices. The baseline evaluation measure is calculated via a classifer (RNN) trained to distinguish real and generated time-series. Particularly, the *discriminative score* equals to the accuracy of such a classifer minus 0.5. Fig. 9, top, shows the results. We conclude that the behaviour of MTop-Div is consistent with the discriminative score: both of them decrease during training. To illustrate training in more details we did PCA projections of real and generated time-series by flattening the time dimension (Fig. 9, bottom). At 2000-th epoch, the point clouds of real (red) and generated (green) time-series became close, which is captured by a drop of MTop-Div score. At the same time, discriminative score is not sensitive enough to this phenomena.

4 Conclusions

We have proposed a tool, Cross-Barcode$_*(P, Q)$, which records multiscale topology discrepancies between two data manifolds approximated by point clouds. Based on the Cross-Barcode$_*(P, Q)$, we have introduced the Manifold Topology Divergence and have applied it to evaluate the performance of GANs in various domains: 2D images, 3D shapes, time-series. We have shown that the MTop-Div correlates well with domain-specific measures and can be used for model selection. Also, it provides insights about the evolution of generated data manifold during training and can be used for early stopping. The MTop-Div score is domain agnostic and does not rely on pre-trained networks. We have compared the MTop-Div against 7 established evaluation methods: FID, discriminative score, MMD, JSD, 1-coverage, IMD, and Geometry score and found that MTop-Div outperforms many of them and captures well subtle differences in data manifolds. Our methodology permits to overcome the known TDA scalability issues and to carry out the MTop-Div calculations on the most recent datasets such as FFHQ, with the size of up to 10^5 and the dimension of up to 10^7.

Acknowledgements

The problem statement was developed in the framework of Skoltech-MIT NGP program. The work of Serguei Barannikov and Evgeny Burnaev was supported by Ministry of Science and Higher Education grant No. 075-10-2021-068. Authors are thankful to Alexei Artemov for help with the 3D shapes experiment.

References

[1] Panos Achlioptas, Olga Diamanti, Ioannis Mitliagkas, and Leonidas Guibas. Learning representations and generative models for 3d point clouds. In *International conference on machine learning*, pages 40–49. PMLR, 2018.

[2] Serguei Barannikov. Framed Morse complexes and its invariants. *Adv. Soviet Math.*, 21:93–115, 1994.

[3] Serguei Barannikov. Canonical Forms = Persistence Diagrams. Tutorial. In *European Workshop on Computational Geometry (EuroCG 2021)*, 2021.

[4] Ulrich Bauer. Ripser: efficient computation of Vietoris–Rips persistence barcodes. *Journal of Applied and Computational Topology*, pages 1–33, 2021.

[5] Mikhail Belkin and Partha Niyogi. Laplacian eigenmaps and spectral techniques for embedding and clustering. In *Proceedings of the 14th International Conference on Neural Information Processing Systems: Natural and Synthetic*, pages 585–591, 2001.

[6] Mikołaj Bińkowski, Dougal J Sutherland, Michael Arbel, and Arthur Gretton. Demystifying mmd gans. *arXiv preprint arXiv:1801.01401*, 2018.

[7] Ali Borji. Pros and cons of gan evaluation measures. *Computer Vision and Image Understanding*, 179:41–65, 2019.

[8] Michael M. Bronstein, Joan Bruna, Yann LeCun, Arthur Szlam, and Pierre Vandergheynst. Geometric deep learning: Going beyond euclidean data. *IEEE Signal Processing Magazine*, 34(4):18–42, 2017.

[9] Angel X Chang, Thomas Funkhouser, Leonidas Guibas, Pat Hanrahan, Qixing Huang, Zimo Li, Silvio Savarese, Manolis Savva, Shuran Song, Hao Su, et al. Shapenet: An information-rich 3d model repository. *arXiv preprint arXiv:1512.03012*, 2015.

[10] Frédéric Chazal and Bertrand Michel. An introduction to topological data analysis: fundamental and practical aspects for data scientists. *arXiv preprint arXiv:1710.04019*, 2017.

[11] Alon Efrat, Alon Itai, and Matthew J Katz. Geometry helps in bottleneck matching and related problems. *Algorithmica*, 31(1):1–28, 2001.

[12] Ian Goodfellow, Yoshua Bengio, Aaron Courville, and Yoshua Bengio. *Deep learning*, volume 1. MIT press Cambridge, 2016.

[13] Ian J. Goodfellow, Jean Pouget-Abadie, Mehdi Mirza, Bing Xu, David Warde-Farley, Sherjil Ozair, Aaron Courville, and Yoshua Bengio. Generative adversarial networks, 2014.

[14] Paulina Grnarova, Kfir Y Levy, Aurelien Lucchi, Nathanael Perraudin, Ian Goodfellow, Thomas Hofmann, and Andreas Krause. A domain agnostic measure for monitoring and evaluating gans. In *Advances in Neural Information Processing Systems*, pages 12092–12102, 2019.

[15] Allen Hatcher. *Algebraic topology*. 2005.

[16] Martin Heusel, Hubert Ramsauer, Thomas Unterthiner, Bernhard Nessler, and Sepp Hochreiter. Gans trained by a two time-scale update rule converge to a local nash equilibrium. In *Advances in neural information processing systems*, pages 6626–6637, 2017.

[17] Tero Karras, Samuli Laine, and Timo Aila. A style-based generator architecture for generative adversarial networks. In *Proceedings of the IEEE conference on computer vision and pattern recognition*, pages 4401–4410, 2019.

[18] Tero Karras, Samuli Laine, Miika Aittala, Janne Hellsten, Jaakko Lehtinen, and Timo Aila. Analyzing and improving the image quality of StyleGAN. In *Proceedings of the IEEE/CVF Conference on Computer Vision and Pattern Recognition*, pages 8110–8119, 2020.

[19] Valentin Khrulkov and Ivan Oseledets. Geometry score: A method for comparing generative adversarial networks. In *International Conference on Machine Learning*, pages 2621–2629. PMLR, 2018.

[20] Kwangho Kim, Jisu Kim, Manzil Zaheer, Joon Kim, Frédéric Chazal, and Larry Wasserman. PLLay: Efficient topological layer based on persistence landscapes. In *34th Conference on Neural Information Processing Systems (NeurIPS 2020)*, 2020.

[21] Tuomas Kynkäänniemi, Tero Karras, Samuli Laine, Jaakko Lehtinen, and Timo Aila. Improved precision and recall metric for assessing generative models. In *33rd Conference on Neural Information Processing Systems (NeurIPS 2019)*, 2019.

[22] Mario Lucic, Karol Kurach, Marcin Michalski, Sylvain Gelly, and Olivier Bousquet. Are gans created equal? A large-scale study. In *Advances in Neural Information Processing Systems*, pages 700–709, 2018.

[23] Michael Moor, Max Horn, Bastian Rieck, and Karsten Borgwardt. Topological autoencoders. In *International Conference on Machine Learning*, pages 7045–7054. PMLR, 2020.

[24] Rodrigo Rojas Moraleda, Nektarios A Valous, Wei Xiong, and Niels Halama. *Computational Topology for Biomedical Image and Data Analysis: Theory and Applications*. CRC Press, 2019.

[25] Partha Niyogi, Stephen Smale, and Shmuel Weinberger. Finding the homology of submanifolds with high confidence from random samples. *Discrete & Computational Geometry*, 39(1-3):419–441, 2008.

[26] Augustus Odena, Christopher Olah, and Jonathon Shlens. Conditional image synthesis with auxiliary classifier gans. In *International conference on machine learning*, pages 2642–2651. PMLR, 2017.

[27] Catherine Olsson, Surya Bhupatiraju, Tom Brown, Augustus Odena, and Ian Goodfellow. Skill rating for generative models. *arXiv preprint arXiv:1808.04888*, 2018.

[28] Suman Ravuri and Oriol Vinyals. Classification accuracy score for conditional generative models. *arXiv preprint arXiv:1905.10887*, 2019.

[29] Tim Salimans, Ian Goodfellow, Wojciech Zaremba, Vicki Cheung, Alec Radford, and Xi Chen. Improved techniques for training gans. *arXiv preprint arXiv:1606.03498*, 2016.

[30] Lucas Theis, Aäron van den Oord, and Matthias Bethge. A note on the evaluation of generative models. *arXiv preprint arXiv:1511.01844*, 2015.

[31] Anton Tsitsulin, Marina Munkhoeva, Davide Mottin, Panagiotis Karras, Alex Bronstein, Ivan Oseledets, and Emmanuel Mueller. The shape of data: Intrinsic distance for data distributions. In *International Conference on Learning Representations*, 2019.

[32] Abdul Waheed, Muskan Goyal, Deepak Gupta, Ashish Khanna, Fadi Al-Turjman, and Plácido Rogerio Pinheiro. Covidgan: data augmentation using auxiliary classifier gan for improved covid-19 detection. *Ieee Access*, 8:91916–91923, 2020.

[33] George W Whitehead. *Elements of homotopy theory*, volume 61. Springer Science & Business Media, 1968.

[34] Jinsung Yoon, Daniel Jarrett, and Mihaela van der Schaar. Time-series generative adversarial networks. 2019.

[35] Simon Zhang, Mengbai Xiao, and Hao Wang. Gpu-accelerated computation of Vietoris-Rips persistence barcodes. In *36th International Symposium on Computational Geometry (SoCG 2020)*. Schloss Dagstuhl-Leibniz-Zentrum für Informatik, 2020.

[36] Afra Zomorodian and Gunnar Carlsson. Computing persistent homology. *Discrete & Computational Geometry*, 33(2):249–274, 2005.

[37] Afra J Zomorodian. *Computing and comprehending topology: Persistence and hierarchical Morse complexes (Ph.D.Thesis)*. University of Illinois at Urbana-Champaign, 2001.

A Simplicial Complexes, Cycles, Barcodes

A.1 Background

The simplicial complex is a combinatorial data that can be thought of as a higher-dimensional generalization of a graph. Simplicial complex S is a collection of $k-$simplices, which are finite $(k+1)-$elements subsets in a given set V, for $k \geq 0$. The collection of simplices S must satisfy the condition that for each $\sigma \in S$, $\sigma' \subset \sigma$ implies $\sigma' \in S$. A simplicial complex consisting only of $0-$ and $1-$simplices is a graph.

Let $C_k(S)$ denotes the vector space over a field F whose basis elements are $k-$simplices from S with a choice of ordering of vertices up to an even permutation. In calculations it is most convenient to put $F = \mathbb{Z}_2$. The boundary linear operator $\partial_k : C_k(S) \to C_{k-1}(S)$ is defined on $\sigma = \{x_0, \ldots, x_k\}$ as

$$\partial_k \sigma = \sum_{j=0}^{k} (-1)^j \{x_0, \ldots, x_{j-1}, x_{j+1}, \ldots, x_k\}.$$

The $k-$th **homology** group $H_k(S)$ is defined as the vector space $\ker \partial_k / \operatorname{im} \partial_{k+1}$. The elements $c \in \ker \partial_k$ are called **cycles**. The elements $\tilde{c} \in \operatorname{im} \partial_{k+1}$ are called boundaries. The general elements $c' \in C_k(S)$ are called chains. The elements of $H_k(S)$ represent various $k-$dimensional topological features in S. A basis in $H_k(S)$ corresponds to a set of basic topological features.

Filtration on simplicial complex is defined as a family of simplicial complexes S_α with nested collections of simplices: for $\alpha_1 < \alpha_2$ all simplices of S_{α_1} are also in S_{α_2}. In practical examples the indexes α run through a discrete set $\alpha_1 < \ldots < \alpha_{\max}$.

The inclusions $S_\alpha \subseteq S_\beta$ induce naturally the maps on the homology groups $H_k(S_\alpha) \to H_k(S_\beta)$. The evolution of the cycles through the nested family of simplicial complexes S_α is described by the barcodes. The persistent homology principal theorem [2, 36, 37] states that for each dimension there exists a choice of a set of basic topological features across all S_α so that each feature appears in $H_k(S_\alpha)$ at specific time $\alpha = b_j$ and disappears at specific time $\alpha = d_j$. The H_i barcode of the filtered simplicial complex is the record of these times represented as the collection of segments $[b_j, d_j]$. The barcodes are defined and calculated through bringing the set of matrices of the boundary operators ∂_k to the "Canonical Form" by a change of the basis in C_k preserving the nested family S_α [2, 3].

Let (Γ, m) be a weighted graph with distance-like weights, where m is the symmetric matrix of the weights attached to the edges of the graph Γ. The Vietoris-Rips filtered simplicial complex of the weighted graph $R_\alpha(\Gamma, m)$, is defined as the nested collection of simplices:

$$R_\alpha(\Gamma, m) = \{\{x_0, \ldots, x_k\}, x_i \in \mathrm{Vert}(\Gamma) \| m(x_j, x_l) \leq \alpha\}$$

where $\mathrm{Vert}(\Gamma)$ is the set of vertices of the graph Γ. Even though such weighted graphs do not always come from a set of points in metric space, barcodes of weighted graphs have been successfully applied in many situations (networks, fmri, medical data, graph's classification etc).

A.2 Simplices, describing discrepancies between the two manifolds

Here we gather more details on the construction of sets of simplicies that describe discrepancies between two point clouds P and Q sampled from the two distributions $\mathcal{P}$, $\mathcal{Q}$. As we have described in section 2, our basic methodology is to add consecutively the edges between $P-$points and $Q-$points and between pairs of $P-$points. All edges between $Q-$points are added simultaneously at the beginning at the threshold $\alpha = 0$. The PP and PQ edges are sorted by their length, and are added at the threshold $\alpha \geq 0$ corresponding to the length of the edge. This process is visualized in more details on Figures 10 and 11. The triangles are added at the threshold at which the last of its three edges are added. The $3-$ and higher $k-$simplices are added similarly at the threshold corresponding to the adding of the last of their edges. The added triangles and higher dimensional simplices are not shown explicitely on Figure 1 for ease of perception, as they can be restored from their edges. As all simplices within the $Q-$cloud are added at the very beginning at $\alpha = 0$, the corresponding cycles formed by the $Q-$cloud simplices are immediately killed at $\alpha = 0$ and do not contribute to the Cross-Barcode.

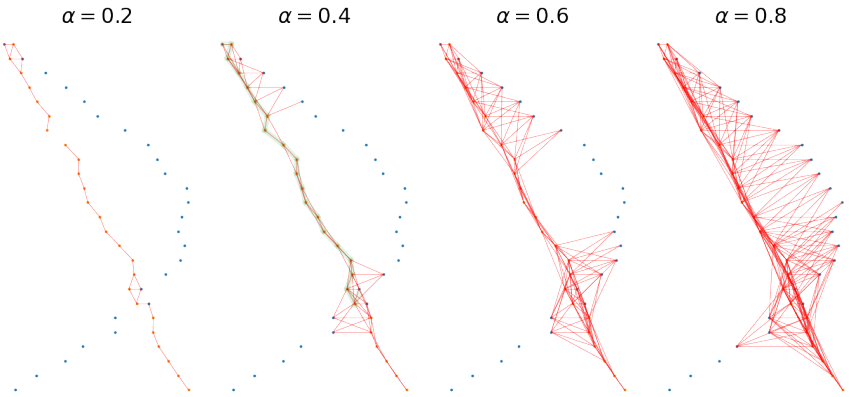

Figure 10: We are adding edges between $P-$points(orange) and $Q-$points(blue) and between pairs of $P-$points consecutively. The edges are sorted by their length, and are added at the threshold $\alpha \geq 0$ corresponding to the length of the edge. Here at the thresholds $\alpha = 0.2, 0.4, 0.6, 0.8$ edges with length less than α were added. For ease of perception the simultaneously added triangles and higher simplices, as well as the added at $\alpha = 0$ all simplices between $Q-$points, are not shown explicitly here. Notice how the $1-$cycle, shown with green, with endpoints in $Q-$cloud is born at $\alpha = 0.4$. It survives at $\alpha = 0.6$ and it is killed at $\alpha = 0.8$.

The constructed set of simplices is naturally a simplicial complex, since for any added $k-$simplex, we have added also all its $(k-1)-$faces obtained by deletion of one of vertices. The threshold α defines the filtration on the obtained simplicial complex, since the simplices added at smaller threshold α_1 are contained in the set of simplices added at any bigger threshold $\alpha_2 > \alpha_1$.

With adding more edges, the cycles start to appear. In our case, a cycle is essentially a collection of simplices whose boundary is allowed to be nonzero if the boundary consists of simplices with vertices from Q. For example, a $1-$ cycle in our case is a path consisting of added edges, that can start and end in $Q-$cloud and that passes through $P-$points. This is because any such collection can be completed to a collection with zero boundary since any cycle from $Q-$cloud is a boundary of a sum of added at $\alpha = 0$ simplices from Q.

A $1-$cycle disappears at the threshold when a set of triangles is added whose boundary coincides with the $1-$cycle plus perhaps some edges between $Q-$points.

Notice how the $1-$cycle with endpoints in $Q-$cloud is born at $\alpha = 0.4$ on Figure 10, shown with green. It survives at $\alpha = 0.6$ and it is killed at $\alpha = 0.8$. The process of adding longer edges can be visually assimilated to the building of a "spider's web" that tries to bring the cloud of red points closer to the cloud of blue points. The obstructions to this are quantified by "lifespans" of cycles, they correspond to the lengths of segments in the barcode. See e.g., Figure 11 where a $1-$cycle is born between $\alpha = 0.5$ and 0.9, it then corresponds to the green segment in the Cross-Barcode.

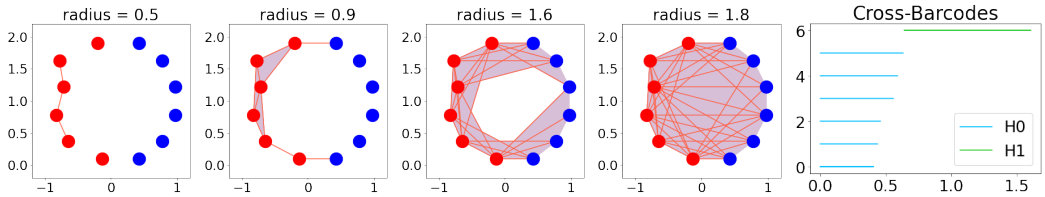

Figure 11: The process of adding the simplices between the $P-$cloud(red) and $Q-$cloud(blue) and within the $P-$cloud. Here we show the consecutive adding of edges together with simultaneous adding of triangles. All the edges and simplices within $Q-$cloud are assumed added at $\alpha = 0$ and are not shown here for perception's ease. Notice the $1-$cycle born between $\alpha = 0.5$ and 0.9, it corresponds to the green segment in the shown Cross-Barcode

Remark A.1. *To characterise the situation of two data point clouds one of which is a subcloud of the other $S \subset C$, it can be tempting to start seeking a "relative homology" analog of the standard (single)*

point cloud persistent homology. The reader should be warned that the common in the literature "relative persistent homology" concept and its variants, i.e. the persistent homology of the decreasing sequence of factor-complexes of a fixed complex: $K \to \ldots K/K_i \to K/K_{i+1} \to \ldots K/K$, is irrelevant in the present context. In contrast, our methodology, in particular, does not involve factor-complexes construction, which is generally computationally prohibitive. The point is that the basic concept of filtered complex contains naturally its own relative analogue via the appropriate use of various filtrations.

A.3 Sub-manifolds and bars in Cross-Barcode$_*(P,Q)$

It is natural to start analyzing the closeness of the data point cloud P to the data point cloud Q by looking at the matrix of the PQ pairwise distances. If there are many points from P such that their distance to their closest point from Q is relatively big then the clouds P and Q are not close. However, in applications, it is important to distinguish the different situations here. The first case is when all these remote from Q points are close to each other. Then this remote from Q cluster of P points represents a single topological feature distinguishing cloud P from Q. Another case is when the remote from Q points form several clusters so that each such remote from Q cluster represents a separate topological feature. The long bars in the zero-dimensional Cross-Barcode record the lifespans on the distances' scale of these remote from Q clusters of $P-$points.

In practice it also happens more often that it is not possible to distinguish a separate cluster of P points which are all remote from Q. Rather, there are some $P-$points inside the same $P-$cluster that are close to Q and other $P-$points from the same $P-$cluster which are further away from Q, as on Fig.1. This situation is captured and quantified by the higher dimensional topological features distinguishing cloud P from Q. Intuitively such an $i-$dimensional topological feature represents an $i-$dimensional $P-$cloud's sub-manifold whose boundary is close to the $Q-$cloud, but whose interior $P-$points are remote from the $Q-$cloud, like the green polygonal chain on Fig.10 at $\alpha = 0.4$. Such features are constructed in the algorithm using the distance matrix combinatorics from $(i+1)-$tuples of $P-$points or P & $Q-$ points. The distances within each of these tuples are less or equal to the feature's appearance, or birth, threshold. The disappearance, or death, of such a feature calculated by the algorithm corresponds approximately to the scale at which the feature becomes indistinguishable from the $Q-$cloud. The $i-$dimensional Cross-Barcode$_i(P,Q)$, $i \geq 1$, is the set of segments (bars) recording the birth and the death thresholds of such topological features.

A.4 Cross-Barcode$_*(P,Q)$ as obstructions to assigning P points to distribution $\mathcal{Q}$

Geometrically, the lowest dimensional Cross-Barcode$_0(P,Q)$ is the record of relative hierarchical clustering of the following form. For a given threshold r, let us consider all points of the point cloud Q plus the points of the cloud P lying at a distance less than r from a point of Q as belonging to the single $Q-$cluster. It is natural to form simultaneously other clusters based on the threshold r, with the rule that if the distance between two points of P is less than threshold r then they belong to the same cluster. When the threshold r is increased, two or more clusters can collide. And the threshold, at which this happens, corresponds precisely to the "death" time of one or more of the colliding clusters. At the end, for very large r only the unique $Q-$cluster survives. Then Cross-Barcode$_0(P,Q)$ records the survival times for this relative clustering.

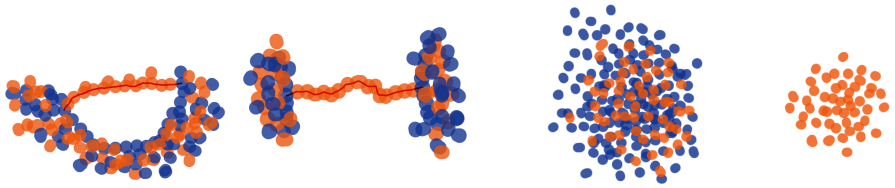

Figure 12: Paths/membranes (red) in the void that are formed by small intersecting disks around P points (orange), and are ending on Q (blue), are obstacles for identification of the distribution $\mathcal{P}$ with $\mathcal{Q}$. These obstacles are quantified by Cross-Barcode$_1(P,Q)$. Separate clusters are the obstacles quantified by Cross-Barcode$_0(P,Q)$.

Notice that in situations, like, for example, in Figure 12, it is difficult to attribute confidently certain points of P to the same distribution as the point cloud Q even when they belong to the "big" $Q-$cluster

at a small threshold r, because of the nontrivial topology. Such "membranes" of $P-$points in void space, are obstacles for assigning points from P to distribution $\mathcal{Q}$. These obstacles are quantified by the segments from the higher barcodes Cross-Barcode$_{\geq 1}(P, Q)$. The bigger the length of the associated segment in the barcode, the further the membrane passes away from Q.

A.5 More simple synthetic datasets in 2D

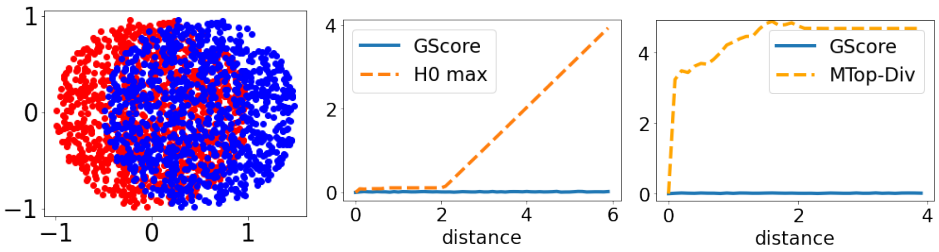

Figure 13: The first picture shows two clouds of 1000 points sampled from the uniform distributions on two different disks of radius 1 with a distance between the centers of the disks of 0.5. The second and third pictures show the dependence of the GScore metric (the GScore is equal to zero independently of the distance between the disks), maximum of segments in $H0$ and the sum of lengths of segments H1 as a function of the distance between the centers of the disks averaged over 10 runs. The length of the maximum segment barcode in H0 grows linearly and equals to the distance between the pair of closest points in the two distributions.

As illustrated on Figures 2,13 the GScore is unresponsive to changes of the distributions' positions.

A.6 Cross-Barcode and precision-recall

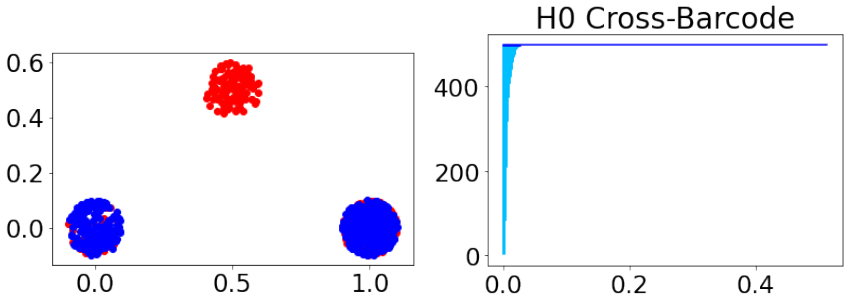

Figure 14: Mode-dropping, bad recall & good precision, illustrated with clouds P_{data} (red) and Q_{model} (blue). The Cross-Barcode$_0(P_{\text{data}}, Q_{\text{model}})$ contains long intervals, one for each dropped mode, which measure the distance from the data's dropped mode to the closest generated mode.

The Cross-Barcode captures well the precision vs. recall aspects of the point cloud's approximations, contrary to FID, which is known to mix the two aspects. For example, in the case of mode-dropping, bad recall but good precision, the Cross-Barcode$_0(P_{\text{data}}, Q_{\text{model}})$ contains the long intervals, one for each dropped mode, which measure the distance from the data's dropped mode to the closest generated mode. The mode-dropping case (bad recall, good precision) is illustrated on Figure 14.

Analogously, in the case of mode-invention, with good recall but bad precision, the Cross-Barcode$_0(Q_{\text{model}}, P_{\text{data}})$ contains long intervals, one for each invented mode, which measure the distance from the model's invented mode to the closest data's mode.

The mode-invention (good recall, bad precision) case is illustrated on Figure 15.

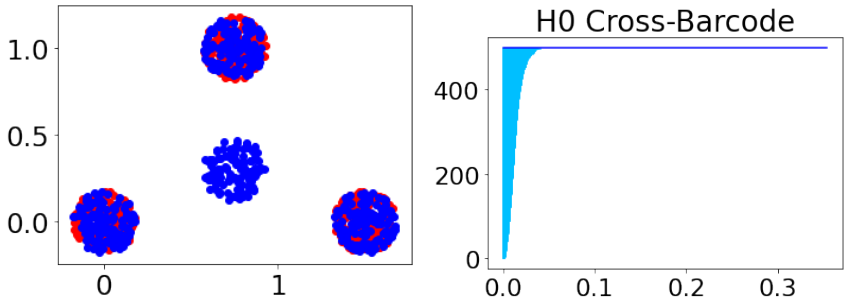

Figure 15: Mode-invention, good recall & bad precision, illustrated with clouds P_{data} (red) and Q_{model} (blue). The Cross-Barcode$_0(Q_{\text{model}}, P_{\text{data}})$ contains long intervals, one for each invented mode, which measure the distance from the model's invented mode to the closest data's mode.

B Cross-Barcode Properties.

B.1 The Cross-Barcode's norm and the Hausdorf distance.

The Bottleneck distance [11], also known as Wasserstein$-\infty$ distance $\mathbb{W}_\infty$, defines the natural norm on the Cross-Barcodes:

$$\|\text{Cross-Barcode}_i\,(P,Q)\|_B = \max_{[b_j,d_j]\in\text{Cross-Barcode}_i}(d_j - b_j).$$

The Hausdorf distance measures how far are two subsets P, Q of a metric space from each other. The Hausdorf distance is the greatest of all the distances from a point in one set to the closest point in the other set:

$$d_{\mathrm{H}}(P,Q) = \max\left\{\sup_{x\in P} d(x,Q),\ \sup_{y\in Q} d(y,P)\right\}. \tag{4}$$

Proposition 1. *The norm of Cross-Barcode$_i(P,Q)$, $i \geq 0$, is bounded from above by the Hausdorff distance*

$$\|\text{Cross-Barcode}_i\,(P,Q)\|_B \leq d_H(P,Q). \tag{5}$$

Proof. Let $c \in R_{\alpha_0}(\Gamma_{P\cup Q}, m_{(P\cup Q)/Q})$ be an $i-$dimensional cycle appearing in the filtered complex at $\alpha = \alpha_0$. Let us construct a simplicial chain that kills c. Let $\sigma = \{x_1, \ldots, x_{i+1}\}$ be one of the simplices from c. Let q_j denote the closest point in Q to the vertex x_j. The prism $\{x_1, q_1, \ldots, x_{i+1}, q_{i+1}\}$ can be decomposed into $(i+1)$ simplices $p_k(\sigma) = \{x_1, x_2, \ldots, x_{k-1}, q_k, \ldots, q_{i+1}\}$, $1 \leq k \leq i+1$. The boundary of the prism consists of the two simplices σ, $q(\sigma) = \{q_1, \ldots, q_{i+1}\}$, and of the $(i+1)$ similar prisms corresponding to the the boundary simplices of σ. If $c = \sum_n a_n\sigma^n$ then

$$c = \partial(\sum_n a_n \sum_k p_k(\sigma^n)) + \sum_n a_n q(\sigma_n)$$

For any k, j, $d(x_j, x_k) \leq \alpha_0$ since c is born at α_0. Therefore

$$d(x_j, q_k) \leq d(x_j, x_k) + d(x_k, q_k) \leq \alpha_0 + \sup_{x\in P} d(x,Q).$$

Therefore all simplices $p_k(\sigma^n))$ appear no later than at $(\alpha_0 + \sup_{x\in P} d(x,Q))$ in the filtered complex. All vertices of the simplices $q(\sigma_n)$ are from Q. It follows that the lifespan of the cycle c is no bigger than $\sup_{x\in P} d(x,Q))$ □

To illustrate the proposition 1 we have verified empirically the diminishing of Cross-Barcode$_*(Q_1, Q_2)$ when number of points in Q_1, Q_2 goes to $+\infty$ and Q_1, Q_2 are sampled from the same uniform distribution on the 2D disk of radius 1. The maximal length of segments in $H1$ as function of number of points in the clouds of the same size is shown in Figure 16.

B.2 MTop-Div and the Cross-Barcode's Relative Living Times (RLT)

The Cross-Barcode for a given homology H_i is a list of birth-death pairs (segments)

$$\text{Cross-Barcode}_i(P,Q) = \{[b_j, d_j]\}_{j=1}^n$$

Relative Living Times is a discrete distribution $RLT(k)$ over non-negative integers $k \in \{0, 1, \ldots, +\infty\}$. For a given $\alpha_{max} > 0$, $RLT(k)$ is a fraction of "time", that is, parts of horizontal axis $\tau \in [0, \alpha_{max}]$, such that exactly k segments $[b_i, d_i]$ include τ.

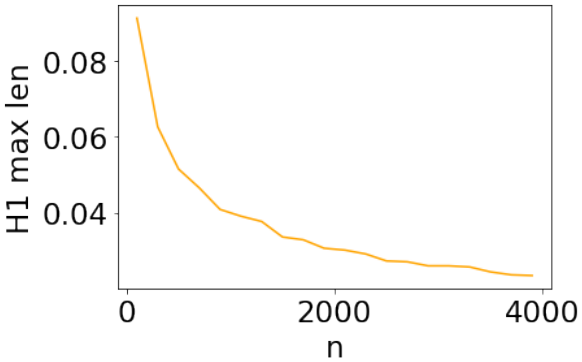

Figure 16: Diminishing of the length of maximal segment in H_1 with increase of the number of sampled points for point clouds of the equal size n sampled from the same uniform distribution on the 2D disk of radius 1.

For equal point clouds, Cross-Barcode$_i(P,P) = \varnothing$ and the corresponding RLT is the discrete distribution concentrated at zero. Let us denote by O_0 such discrete distribution corresponding to the empty set. A natural measure of closeness of the distribution RLT to the distribution O_0 is the earth-mover's distance (EMD), also called Wasserstein-1 distance.

Proposition. Let for all $d_i \leq \alpha_{max}$, then

$$\text{MTop-Div}(P,Q) = \alpha_{max}\text{EMD}(RLT(k), O_0).$$

Proof. By the definition of EMD

$$\text{EMD}(RLT, O_0) = \sum_{k=1}^{+\infty} k \times RLT(k).$$

Let's use all the distinct b_i, d_i to split $[0, \alpha_{max}]$ to disjoint segments s_j:

$$[0, \alpha_{max}] = \bigsqcup_j s_j.$$

Each s_j is included in $K(j)$ segments $[b_i, d_i]$ from the Cross-Barcode$_i(P,Q)$. Thus,

$$RLT(k) = \frac{1}{\alpha_{max}} \sum_{j:K(j)=k} |s_j|.$$

At the same time:

$$\text{MTop-Div}(P,Q) = \sum_i (d_i - b_i) = \sum_j K(j)|s_j| = \sum_{k=1}^{+\infty} \sum_{j:K(j)=k} K(j)|s_j|$$
$$= \sum_{k=1}^{+\infty} \alpha_{max} \times k \times RLT(k) = \alpha_{max}\text{EMD}(RLT(k), O_0).$$

□

C Hyperparameters, Software used, and Experiments' Details

We have made experiments in various settings and on the following datasets:

- on a set of gaussians in 2D in comparison with distributions generated by GAN and WGAN.
- **MNIST** We have observed that GScore is not sensitive to the flip of the cloud of "fives", while our score MTop-Divergence is sensitive to such flip since it depends on the positions of clouds with respect to each other

- **CIFAR10** We have evaluated our MTop-Div(D,M) using a benchmark with the controllable disturbance level. We have observed that Geometry Score is monotone only for 'mode invention' and 'intra-mode collapse' while MTop-Div(D,M) is almost monotone for all the cases.
- **FFHQ** We have evaluated the quality of distributions generated by StyleGAN and StyleGAN-2, without truncation and with $\psi = 0.7$ truncation. We observed that the ranking via MTop-Div is consistent with FID
- **ShapeNet**[6] We have studied the training dynamics of the GAN trained on 3D shapes. We observed that MTop-Div is consistent with domain specific measures (JSD, MMD, Coverage) and that MTop-Div better describes the evolution of the point cloud of generated objects during epochs;
- **Stock data** We have studied the training dynamics of TimeGAN [7] applied to market stock data. We observed that MTop-Div is consistent with the discriminative score but better captures the evolution of point cloud of generated objects during epochs;
- **Chest X-ray images** We have studied the training dynamics of ACGAN applied to chest X-ray images. We observed that MTop-Div is more consistent with the discriminative score than FID;

For computation of FID we used Pytorch-FID[8]. For computation of Geometry Score we used the original code[9] patched to supported multi-threading, otherwise it was extremely slow. The RLTs computation was averaged over 2500 trials. We calculated persistent homology via ripser++[10].

We used the following hyperparameters to compute MTop-Div:

- MNIST: $b_P = 10^2, b_Q = 10^3$;
- Gaussians: $b_P = 10^2, b_Q = 10^3$;
- CIFAR10: $b_P = 10^3, b_Q = 10^4$;
- FFHQ: $b_P = 10^3, b_Q = 10^4$.
- ShapeNet: $b_P = 10^2, b_Q = 10^3$;
- Market stock data: $b_P = 10^2, b_Q = 10^3$;
- Chest X-ray data: $b_P = 10^2, b_Q = 10^3$.

MTop-Div scores were were averaged over 20 runs.

We compared Geometry Score and MTop-Div in the experiment with mixtures of Gaussians. Table 4 shows the results. We conclude that the MTop-Div is consistent with the visual quality of GAN's output while Geometry Score fails.

Figure 17 shows Cross-Barcodes for the experiment with StyleGAN's trained on FFHQ. Figure 19 shows one of Cross-Barcodes in H_0 from the experiment with CIFAR10 dataset to illustrate that the $0-$dimensional Cross-Barcode can also be applied. Figure 18 shows the Cross-Barcodes in H_1 from the experiments with GAN[11] and WGAN-GP [12] trained on mixture of Gaussians.

Table 3 shows extended experimental results on GAN model selection including standard error of sample means of MTop-Div.

Figure 20 presents real and generated chest X-ray images. The generated images are of high visual quality and resembles real images.

Figure 21 shows real and generated 3D shapes. Generated 3D shapes (bottom row) are relatively blurry.

[6] The dataset is free for non-commercial purposes.
[7] `https://github.com/jsyoon0823/TimeGAN`
[8] `https://github.com/mseitzer/pytorch-fid`, (Apache Licence 2.0)
[9] `https://github.com/KhrulkovV/geometry-score`
[10] `https://github.com/simonzhang00/ripser-plusplus`, (MIT License)
[11] https://arxiv.org/abs/1406.2661
[12] https://arxiv.org/abs/1704.00028

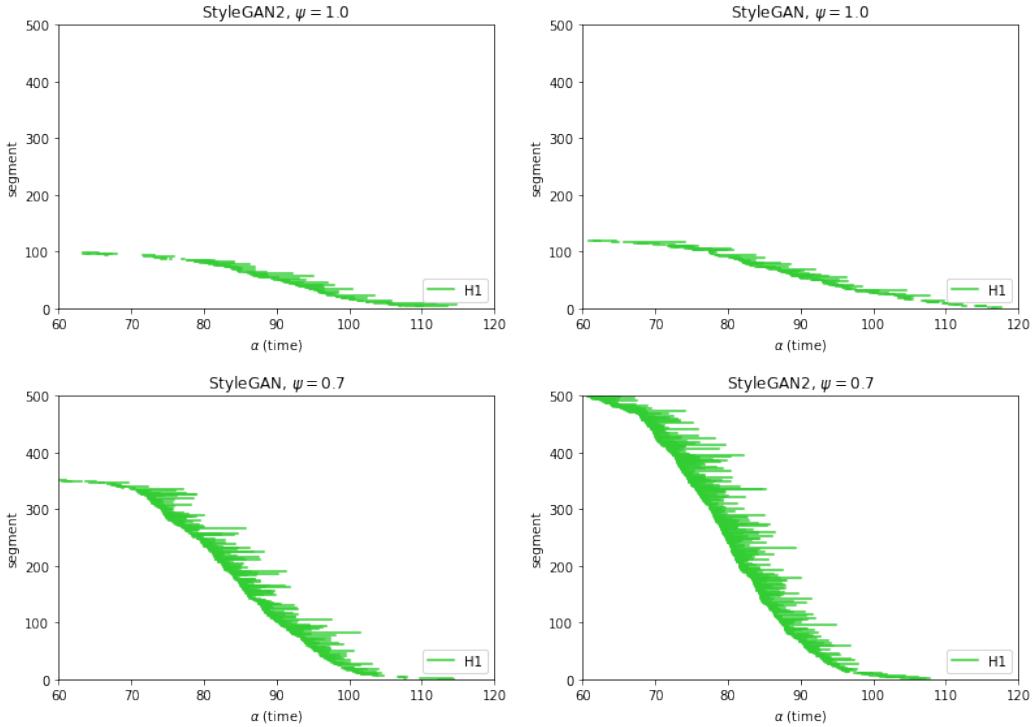

Figure 17: Cross-Barcodes for GAN's trained on FFHQ. Cross-Barcodes are shown by decrease of generator performance. For clarity, only H_1 barcodes are shown. The number and the total length of segments give the same ranking as the FID score

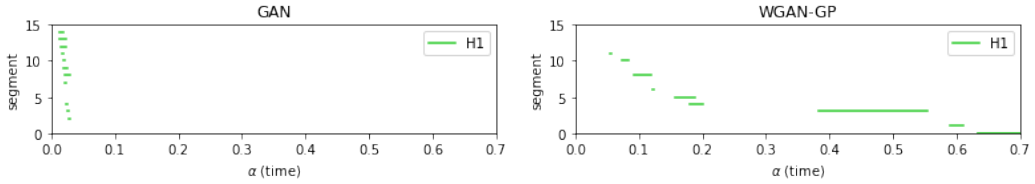

Figure 18: Cross-Barcodes for GAN's trained of mixtures of Gaussians. Cross-Barcodes are shown by decrease of generator performance. For clarity, only H_1 barcodes are shown.

D MTop-Div for Cross-Barcodes of higher order

We calculated MTop-Div$_k$(D,M) based on higher order Cross-Barcodes, that is, sums of segments' lengths of Cross-Barcode$_k$, $k > 1$ were taken in Algorithm 2. Then, we measured average Kendall-tau rank correlation between MTop-Div$_k$(D,M) and the disturbance level for the series of synthetic modifications of CIFAR10. For MTop-Div$_2$(D,M) the rank correlation was 0.59, for MTop-Div$_3$(D,M): 0.45. To make faster calculations small batches were selected, MTop-Div$_2$(D,M): $b_P = 100, b_Q = 300$, MTop-Div$_3$(D,M): $b_P = 100, b_Q = 100$. An optimization that we describe in a future publication pre-computes the unnecessary simplices and permits faster higher degree MTop-Div computations.

Table 2: Performance measures of StyleGANs trained on FFHQ.

GAN	ψ	FID	MTOP-DIV(M,D)
STYLEGAN2	1.0	4.75	162.08
STYLEGAN	1.0	8.25	234.33
STYLEGAN	0.7	15.86	712.57
STYLEGAN2	0.7	19.75	1011.53

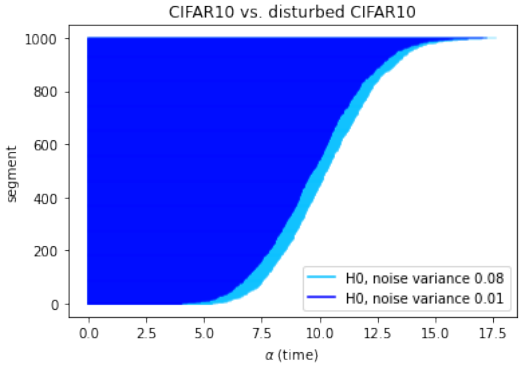

Figure 19: Cross-Barcodes for CIFAR10 vs. disturbed CIFAR10. Gaussian noise with 2 levels of variance was applied. For clarity, only H_0 barcodes are shown. For ease of perception of differences in Cross-Barcodes$_0$ they are shown on the same plot. The dataset with higher level of noise is distinguished here by the longer segments in the Cross-Barcode$_0$

Table 3: MTop-Div is consistent with FID for model selection of GAN's trained on various datasets.

Dataset	FID		MTop-Div(M,D)	
	WGAN	WGAN-GP	WGAN	WGAN-GP
CIFAR10	**154.6**	399.2	**370.5±17.3**	2408.5±27.0
SVHN	**101.6**	154.7	**332.0±12.4**	963.2±22.62
MNIST	31.8	**22.0**	2365.6±40.1	**1474.2±29.7**
FashionMNIST	52.9	**35.1**	1052.6±24.8	**872.9±21.8**

E Comparison with the "Intrinsic Multi-scale Distance(IMD)"

As proposed by a reviewer, we did additional experiments with IMD [31] applied to point clouds from our experiments. IMD is not sensitive to the rings shift (Section 3.1) and the digits flipping on MNIST (Section 3.3). For the experiment "Mode dropping on Gaussians" (Section 3.2), IMD incorrectly ranks poorly performing WGAN-GP (see Fig.3) higher than the original GAN (Table 4). For the experiments "GAN model selection" (Section 3.5), IMD ranks a better performing model lower in one case, while the ranking via MTop-Div is consistent with true GAN performance. For the "Synthetic variations of CIFAR10" experiment (Section 3.4), the average Kendall-tau correlation between IMD score and the disturbance level is 0.55, which is lower than the same measure of MTop-Div (0.89).

Table 4: MTop-Div and G. Score for GAN's trained of mixtures of Gaussians.

GAN	G. SCORE	MTOP-DIV(M,D)	MTOP-DIV(D,M)	IMD
WGAN-GP	**1.083**	0.562	0.206	**2.65**
ORIG. GAN	1.087	**0.081**	**0.149**	13.87

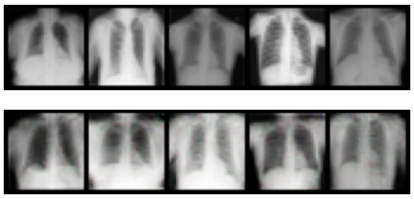

Figure 20: Top: real chest X-ray images. Bottom: generated chest X-ray images.

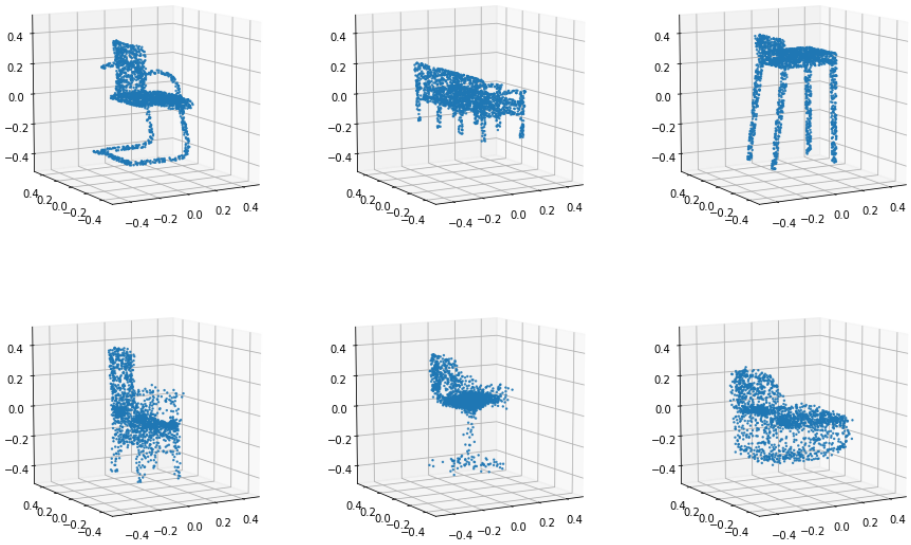

Figure 21: Top: real 3D shapes. Bottom: generated 3D shapes. Generated 3D shapes are relatively blurry.